AIAA JOURNAL
Vol. 36, No. 7, July 1998

Computations of Steady and Unsteady Low-Speed Turbulent Separated Flows

Reece E. Neel,* Robert W. Walters,† and Roger L. Simpson‡
Virginia Polytechnic Institute and State University, Blacksburg, Virginia 24061

Numerical computations are presented for two-dimensional steady and unsteady separated flows. The first case is a low-speed, converging–diverging duct with a rapid expansion, creating a large separated flow region. The second case is the Massachusetts Institute of Technology flapping foil experiment, where a stationary hydrofoil is subject to gust loading. Numerical solutions are obtained by solving the incompressible Navier–Stokes equations. These equations are solved in a time accurate manner using the method of artificial compressibility. The Johnson and King (Johnson, D. A., and King, L. S., "A Mathematically Simple Turbulence Closure Model for Attached and Separated Turbulent Boundary Layers," *AIAA Journal*, Vol. 23, No. 11, 1985, pp. 1684–1692) turbulence model is employed for modeling the turbulent flow. Modifications to the model are suggested that take into account the normal stress production of energy and the strong adverse pressure gradient associated with separating flows. The performance of the Johnson and King model and its modifications are studied for both steady and unsteady flow conditions. The numerical solutions are compared to experimental data.

Nomenclature

A^+ = van Driest damping constant
D = near-wall damping term
$\mathcal{D}$ = turbulent diffusion rate
F = ratio of total turbulence energy production to shear stress production
K = Clauser modeling constant, set to 0.0168
L = dissipation length scale
p = pressure
q^2 = turbulent flow property, $u'^2 + v'^2 + w'^2$
u, v = mean flow Cartesian velocities in the x and y directions
u^* = wall shear velocity
u_s = turbulence model velocity scale parameter
x, y = Cartesian coordinates
y^+ = yu^*/ν
β = artificial compressibility parameter
γ = Klebanoff's intermittency function
Δt = physical time step
$\Delta\tau$ = pseudotime step (nonphysical time step)
δ = boundary-layer thickness
δ^* = boundary-layer displacement thickness
θ = contravariant velocity
κ = von Kármán's constant
μ = molecular viscosity
μ_t = turbulent eddy viscosity
ν = dynamic viscosity, μ/ρ
ρ = density
σ = ratio of actual to equilibrium τ_m
τ = Reynolds shear stress, $(-\rho\overline{u'v'})$
τ_w = wall shear stress

Subscripts

e = boundary-layer edge conditions
eq = equilibrium conditions
i = inner part of boundary layer
m = values of quantity where τ is a maximum
o = outer part of boundary layer

Superscripts

m = pseudotime level
n = physical time level
$()'$ = fluctuating quantity

Presented as Paper 97-0653 at the AIAA 35th Aerospace Sciences Meeting, Reno, NV, Jan. 6–9, 1997; received March 5, 1997; revision received March 8, 1998; accepted for publication April 1, 1998.

*Graduate Research Assistant, Department of Aerospace and Ocean Engineering. Student Member AIAA.
†Professor, Department of Aerospace and Ocean Engineering. Associate Fellow AIAA.
‡Jack E. Cowling Professor, Department of Aerospace and Ocean Engineering. Fellow AIAA.

Introduction

REGIONS of separated flow are common in many engineering applications. Separation is the entire process in which the boundary-layer flow breaks down and departs from the wall surface. This physical phenomenon can have a large impact on the performance of any design. It is often possible to avoid separation by placing limitations on the operating conditions. However, there are times when separated flow cannot be avoided and must, therefore, be dealt with. In these situations it is important to know and understand the effects of separation on a particular design.

There are many turbulence models available, but very few work well in regions of strong adverse pressure gradients or separation. The Johnson and King[1] model (JKM) is one particular formulation that is specifically designed for flows with strong adverse pressure gradients. The model has been shown to work well inside regions of separated flow[2] because it takes into account the nonequilibrium flow development that occurs when a boundary layer changes rapidly.

The first calculated test case in this paper is a low-speed diffuser flow studied by Simpson et al.[3] and was used as a test case for the 1980–1981 AFOSR–HTTM–Stanford conference on complex turbulent flows. The diffuser decelerates the flow rapidly producing a large adverse pressure gradient. This causes the boundary layer to undergo massive separation. All computations are done in regions where the flow remains predominately two dimensional.

This same test case was used by Johnson and King[1] in validating their turbulence model. Only the steady case was computed, and the results were found to agree well with experimental data. In their computations, Johnson and King used an inverse boundary-layer method to solve the separated flow region. The present paper performs this same calculation except with the use of the full incompressible Navier–Stokes equations. In the present case, all of the boundary-layer properties are calculated, whereas in the inverse method some of the parameters are prescribed as part of the boundary-layer edge conditions.

The second test case comes from an experiment performed at the Massachusetts Institute of Technology (MIT) and is known as

the flapping foil experiment (FFX). FFX was performed to simulate blade loading under oscillatory conditions. The unsteady flowfield acting on the blade is modeled in the experiment as a vertical or transverse sinusoidal gust. This unsteady loading on a propeller blade is experienced on ships as the blade rotates through the wake created by the hull or appendage.

The first computational results of this experiment were presented at the March 1993 Office of Naval Research/MIT Unsteady-Flow Workshop. At this meeting, computational results were submitted with only the experimental conditions and boundary data known beforehand. Since then, the experimental data have been released, and additional computations have been performed.[4–7] A variety of turbulence models were used in the computations, but the author is unaware of any results that have previously used the JKM.

Governing Equations

The governing equations used in the numerical computations are the incompressible Navier–Stokes equations. These equations are based on the conservation of mass and momentum. The Reynolds-averaged equations in two-dimensional, Cartesian tensor form are given as

$$\frac{\partial u_i}{\partial x_j} = 0 \tag{1}$$

$$\frac{\partial u_i}{\partial t} + \frac{\partial u_i u_j}{\partial x_j} = \frac{-1}{\rho}\frac{\partial p}{\partial x_j} + \frac{1}{\rho}\frac{\partial}{\partial x_j}\left[\mu\left(\frac{\partial u_j}{\partial x_i} + \frac{\partial u_i}{\partial x_j}\right) + \rho\overline{u_i' u_j'}\right] \tag{2}$$

where u' is the fluctuation velocity about the mean flow. To bring closure to the system, the Boussinesq assumption is used to introduce the eddy viscosity μ_t. The turbulent Reynolds stress is

$$-\rho\overline{u_i' u_j'} = \mu_t\left(\frac{\partial u_j}{x_i} + \frac{\partial u_i}{x_j}\right) \tag{3}$$

The solution algorithm used to solve the governing equations is based on the scheme by Rogers and Kwak.[8,9] The algorithm employs the method of artificial compressibility in which an artificial compressibility parameter β is introduced into the continuity equation along with a time-derivative term for the pressure:

$$\frac{1}{\beta}\frac{\partial p}{\partial \tau} + \frac{\partial u}{\partial x} + \frac{\partial v}{\partial y} = 0 \tag{4}$$

The addition of the pseudotime-derivativeterm directly couples the pressure and velocity. The set of governing equations (2) and (4) become hyperbolic in space–time, which is the same form as the compressible equations. This similarity allows the methods used in solving the compressible equations to be directly applied to the incompressible equations presented here. The equations are solved by marching the solution in physical time. For steady-state solutions, the pseudotime-derivative term will vanish as the solution converges, satisfying the conservation of mass. For time-dependent flows, subiterations are performed, which will satisfy continuity for each physical time step. More details on the solution procedure can be found in Ref. 10.

Turbulence Model

The Johnson and King turbulence model is known as a half-equation model. It is composed of an algebraic eddy viscosity formulation and a differential equation. For steady flows, the equation reduces to an ordinary differential equation (ODE). The differential equation describes the streamwise development of the maximum Reynolds shear stress and is used to scale the eddy viscosity in the outer portion of the boundary layer. The scaling takes into account the nonequilibrium effects when the flow changes rapidly, as in the case of a strong adverse pressure gradient. Nonequilibrium conditions occur when the turbulence production no longer equals the turbulent dissipation of energy. Under these conditions the traditional eddy viscosity models fail to correctly predict the actual flow physics. The JKM is specifically intended to model flows with strong adverse pressure gradients or flows where separation is present.

For the baseline JKM, the eddy viscosity is defined as

$$\nu_t = (\mu_t/\rho) = \nu_{to}[1 - \exp(-\nu_{ti}/\nu_{to})] \tag{5}$$

where ν_{to} and ν_{ti} are the outer and inner viscosities, respectively, and are defined by

$$\nu_{to} = \sigma(x) K U_e \delta^* \gamma \tag{6}$$

$$\nu_{ti} = D^2 \kappa y u_s \tag{7}$$

This provides for a smooth blending of the inner and outer viscosities. In the preceding equations, the near-wall damping term is defined as $D = 1 - \exp(-yu_D/\nu A^+)$. The velocity parameter u_s is scaled on both the Reynolds shear stress and the wall shear velocity.[11] A blending between the two velocity scales is used for a smooth transition. The equation for u_s is

$$u_s = u^*(1 - \gamma_2) + (-\overline{u'v'}_m)^{\frac{1}{2}}\gamma_2 \tag{8}$$

where the term γ_2 is given as $\gamma_2 = 1 - \exp(-y/L_c)$ and u^* is the wall shear velocity. The term L_c is given by

$$L_c = \frac{u^* y_m}{u^* + (-\overline{u'v'}_m)^{\frac{1}{2}}} \tag{9}$$

and, finally, u_D is

$$u_D = \max\left[u^*, (-\overline{u'v'}_m)^{\frac{1}{2}}\right] \tag{10}$$

The subscript m indicates that the variable is evaluated at the y location where the Reynolds shear stress is a maximum. The maximum shear stress location will vary in the streamwise direction. The value of A^+ is 15, K is 0.0168, and von Kármán's constant κ is 0.40.

The JKM requires the solution of the following differential equation for the maximum Reynolds shear stress:

$$\frac{L_m}{\tau_m a_1}\left(\frac{\partial \tau_m}{\partial t} + \bar{u}_m\frac{\partial \tau_m}{\partial x}\right) = \left(\frac{\tau_{m,\mathrm{eq}}}{\rho}\right)^{\frac{1}{2}} - \left(\frac{\tau_m}{\rho}\right)^{\frac{1}{2}} - \frac{\rho L_m \mathcal{D}_m}{\tau_m} \tag{11}$$

where $\tau_m = (-\rho\overline{u'v'})_m$ and the turbulent diffusion term D_m is given by

$$\mathcal{D}_m = \frac{C_{\mathrm{dif}}(\tau_m/\rho)^{\frac{3}{2}}}{a_1\delta[0.7 - (y/\delta)_m]}\left|1 - \sigma(x)^{\frac{1}{2}}\right| \tag{12}$$

This partial differential equation will reduce to an ODE if the time-dependent term is dropped, which is normally the case. The time-derivative term is left here to study the effect it has on time-accurate solutions. The variable $\tau_{m,\mathrm{eq}}$ represents the equilibrium value of the maximum Reynolds shear stress and is found by setting $\sigma(x) = 1$.

In the preceding equations, C_{dif} is a modeling constant taken as 0.5 and L_m is a dissipation length scale. This length scale is based on the maximum Reynolds shear stress height for the inner region and the boundary-layer thickness for the outer region. The values for L_m are

$$L_m = 0.4 y_m, \qquad y_m/\delta \le 0.225 \tag{13}$$

$$L_m = 0.09\delta, \qquad y_m/\delta > 0.225 \tag{14}$$

The differential equation is used to control the value of σ at each streamwise location in the flow. Therefore, only ν_{to} is affected by the solution of the differential equation. This makes the outer eddy viscosity strongly dependent on the development of the Reynolds shear stress instead of just the mean velocity profile. The eddy viscosity model is used to determine the shear stress, and the differential equation is then used to control the level of the shear stress through the σ parameter. At each x location, a value of σ is used to scale Eq. (6) such that the following relationship is satisfied:

$$\nu_{t,m} = \frac{(-\overline{u'v'})_m}{(\partial u/\partial y)_m} \tag{15}$$

This relationship can be satisfied by updating $\sigma(x)$ for each iteration by the following equation:

$$\sigma(x)^{n+1} = \sigma(x)^n \frac{\tau_{m,\mathrm{ODE}}}{\tau_{m,\mathrm{actual}}} \tag{16}$$

Modifications to the JKM

Modifications made to the baseline Johnson and King turbulence model are now discussed. These modifications are either changes made to the existing turbulence model or additional terms added to the JKM. A change is also proposed to the modeling of the Reynolds normal stress in the momentum equations. All of these modifications fall into three categories (discussed subsequently), which help clarify the presentation of each change or addition made.

Changes will first be presented that deal with the outer region eddy viscosity model. These changes will focus on the differential equation used to compute the scaling parameter σ. Next an addition to the turbulence modeling is suggested that is independent of the JKM. This new term is a model for the normal stress that appears in the x-momentum equation after Reynolds averaging. Finally, changes to the inner region will be discussed. A new velocity scale will be proposed, along with a term that is added to the inner model. The added term will focus on effects from the pressure gradient.

Outer Region JKM

It has been observed from experiment[3] that the normal stress production term becomes important in regions of strong adverse pressure gradient and separation. In these regions, the normal stresses can contribute as much as 30% or more of the total turbulent energy production. The ratio of the total turbulence energy production to shear stress production is defined as

$$F = 1 - \frac{(\overline{u'^2} - \overline{v'^2})\partial U/\partial x}{-\overline{u'v'}\partial U/\partial y} \tag{17}$$

Shiloh et al.[12] use the F factor at $-\overline{u'v'}_m$ to make the following correlation between the Reynolds shear stress and the turbulent kinetic energy (TKE):

$$\left(\frac{-\overline{u'v'}}{\overline{q^2}}\right)F^{\alpha} = A_2 = 0.15 \tag{18}$$

where α is best approximated by 1.25 from experimental observations.[12] An expression is also given for the normal stresses relating F and $\overline{q^2}$ as

$$\overline{u'^2} - \overline{v'^2} = \left(\frac{C_2\overline{q^2}}{F^{0.25}}\right) \tag{19}$$

Using Eqs. (17–19), F can be rewritten as the following:

$$F = \left(1 + \frac{C_2}{A_2}\frac{\partial U/\partial x}{\partial U/\partial y}\right)^{-1} \tag{20}$$

where the ratio C_2/A_2 was determined from experiment[12] to have an average value of 2.79.

The equation for the maximum Reynolds shear stress as given in Eqs. (11) and (12) does not take into account production from the normal stresses, but only the shear stresses. To include the normal stress terms, several modifications are made to Eq. (11). Johnson and King used the assumption that $\tau_m/(\rho k_m) = 0.25$, which leaves out the F factor. In this work, the following substitution is made instead:

$$\tau_m/(\rho k_m) = 2A_2/F^{\alpha} \tag{21}$$

where again A_2 has the value of 0.15. The second modification is in the shear production term given by $(\tau_m/\rho)\partial U/\partial y$. This term can be multiplied by the F factor to take into account the normal stress contributions to the production, giving

$$\frac{F\tau_m}{\rho}\frac{\partial U}{\partial y} \tag{22}$$

These corrections are made to Eq. (11), which can now be written as

$$\frac{L_m\bar{u}_m F^{\alpha}}{2\tau_m A_2}\frac{\partial \tau_m}{\partial x} = F\left(\frac{\tau_{m,\mathrm{eq}}}{\rho}\right)^{\frac{1}{2}} - \left(\frac{\tau_m}{\rho}\right)^{\frac{1}{2}} - \frac{\rho L_m \mathcal{D}_m}{\tau_m} \tag{23}$$

where the time-dependent term has been dropped for simplicity. It was observed that this modification, when used throughout the flow, caused separation to occur earlier than the baseline JKM. If Eq. (23) was used only when backflow was present, then the model had less impact on the detachment location ($C_f = 0$) and more emphasis on the backflow region. Therefore, the modified ODE was used in the JKM only in the separated regions where backflow was present.

Momentum Equation

Another location where the normal stresses can be considered is in the Reynolds-averaged Navier–Stokes equations. In the x-momentum equation, two terms appear after performing Reynolds averaging. These two terms appear on the left-hand side of the equation as

$$\frac{\partial(\overline{-u'v'})}{\partial y} + \frac{\partial(\overline{-u'^2})}{\partial x} \tag{24}$$

and can be considered as the gradient of the apparent shearing and normal stresses, respectively. A new approximation is made to better model the normal stress effects. From Eqs. (18) and (19), an expression can be formed for the normal stress term. For strong adverse pressure gradients and separated flows, the following equation is given:

$$\overline{u'^2} - \overline{v'^2} = (C_2/A_2)F(\overline{-u'v'}) \tag{25}$$

Observing the experimental data for the present diffuser flow being studied, the normal stresses from u are around 60% larger than those stresses from v (Ref. 12). It is also observed that the normal stresses only become large in the outer portion of the boundary layer.[13] Using these two observations, the following model was made for the normal stress term:

$$\frac{\partial(\overline{-u'^2})}{\partial x} = -\frac{C_2}{A_2}\frac{\partial}{\partial x}[F(\overline{-u'v'})] \tag{26}$$

The normal stress contributions from this model are added to all locations above the maximum Reynolds shear stress location y_m and set to zero for all locations below it. This was done to be consistent with the experimental observation that the normal stresses are important in the vicinity of the maximum shear stress and above but become small compared to the shear stresses below this location.

Inner Region JKM

The inner region velocity scale parameter u_s was originally set to $(-\overline{u'v'}_m)^{1/2}$ by Johnson and King[1] but was later modified by Johnson and Coakley[11] to improve the near-wall profiles. This modification to the turbulence model, which is given by Eq. (8), was used in the present computations as the baseline JKM. The term u_s was improved by Johnson and Coakley, making it a function of the parameters u^* and $(-\overline{u'v'}_m)^{1/2}$. The reason for the improvement is due to the growth of $(-\overline{u'v'}_m)^{1/2}$ as separation is reached, giving a higher value for μ_{ti}. The wall shear velocity will not grow in magnitude due to separation, making a combination of the two parameters a better choice for the velocity scale. It was found that changing the value of u_s can have a large impact on the profiles and the detachment location. It is not clear what the best parameter is for the inner region velocity scale that will capture the physics of the flow, but it was observed that the local value of the Reynolds shear stress could be used instead of a constant maximum value.[14]

The second modification to the inner eddy viscosity is based on the pressure gradient. To develop a relation that involves the pressure, it is helpful to start with the mean flow momentum equation for steady, two-dimensional flow, which is written as

$$U\frac{\partial U}{\partial x} + V\frac{\partial U}{\partial y} = -\frac{1}{\rho}\frac{\partial P}{\partial x} + \nu\frac{\partial^2 U}{\partial y^2} + \frac{1}{\rho}\frac{\partial(-\rho\overline{u'v'})}{\partial y} \tag{27}$$

Coles integrated this equation (as described in Ref. 15) with respect to y^+ to give the following:

$$\frac{\tau_l + \tau_t}{\tau_w} = 1 + \frac{y}{\rho u^{*2}}\frac{\partial P}{\partial x} + \frac{\nu}{u^{*2}}\frac{\mathrm{d}u^*}{\mathrm{d}x}\int_0^{y^+} h^2(y^+)\,\mathrm{d}y^+ \tag{28}$$

where $h(y^+) = (u/u^*)$. Solving for the turbulent shear stress and keeping all of the terms gives the following equation:

$$\tau_t = \tau_w \left[1 + \frac{y}{\rho u^{*2}} \frac{\partial P}{\partial x} + \frac{\nu}{u^{*2}} \frac{\mathrm{d}u^*}{\mathrm{d}x} \int_0^{y^+} h^2(y^+)\, \mathrm{d}y^+ \right] - \tau_l \quad (29)$$

For most flows, it is common to neglect the pressure gradient and the integral term. Also note that, for the inner logarithmic region, τ_l is much smaller than the turbulent stress τ_t. If these three terms are neglected, then what remains is simply $\tau_t = \tau_w$. This approximation forms the basis for most algebraic turbulence models, such as the Baldwin–Lomax model (BLM), the Cebeci–Smith model, and even the JKM. Instead of neglecting the pressure gradient term in Eq. (29), it will be kept intact to see the impact on the inner region model.

The eddy viscosity formulation states that $\tau_t = \mu_t \partial U/\partial y$. The velocity gradient in the log region can be replaced with $(u^*/\kappa y)$, which comes from the law of the wall. With these substitutions and neglecting the integral and laminar viscosity terms, Eq. (29) becomes

$$\mu_t = \kappa \rho u^* y + \kappa \rho u^* y \left(\frac{y}{\rho u^{*2}} \frac{\partial P}{\partial x} \right) \quad (30)$$

If the first term on the right-hand side is multiplied by the near-wall damping term D and the velocity scale parameter is substituted in for u^*, then this term becomes the inner eddy viscosity for the JKM. The second term is multiplied by the wall damping term as well to give the following equation for the inner eddy viscosity:

$$\nu_{ti} = \nu_{ti\,(JKM)} + \kappa u^* y D \left(\frac{y}{\rho u^{*2}} \frac{\partial P}{\partial x} \right) \quad (31)$$

where the equation was divided through by the density. Note that the additional term in Eq. (31) was made based on law-of-the-wall assumptions. For this reason, the pressure term is set to zero inside the backflow region, where the law of the wall is not valid. It was also found that when using the additional pressure gradient term, the wall shear velocity was the best choice for u_s.

Computed Results: Diffuser

The results presented here are for the steady low-speed diffuser flow. The length of the experimental test section was 7.62 m. Figure 1 shows a diagram of the computational region. From experiment, the fully developed separation location occurs at 3.55 m. The separated region continues to grow and remains strongly two dimensional up to 4.34 m. At this streamwise location, the flow is still separated and the boundary layer occupies over 60% of the test section height. Because of the three-dimensional nature of the flow beyond this location, the computational domain ends at this location. The Reynolds number based on the entrance conditions is 9.6×10^6/m.

The computational grid for this flow consisted of 80 cells in the streamwise direction and 100 cells in the direction normal to the flow. A grid convergence study was performed using the following grid dimensions: (81×51), (81×101), (101×81), and (161×101). Parameters such as the boundary-layer edge velocity, the skin-friction coefficient, and velocity profiles in the separated region were compared, with the conclusion that the (81×101) mesh provided the necessary resolution. The clustering of cells next to the viscous wall was done such that the smallest value of y^+ was less than one. The upper wall boundary was treated as a streamline, which was determined at the time of the experiment. The lower wall was treated with the no-slip condition. The inflow boundary used the u and v experimental data to set the velocity profile. Pressure at the inflow was extracted from the interior cells. The outflow boundary for the diffuser was slightly more complex because it occurred inside the separated region. Where the flow was reversed and entered back into the domain (backflow velocity), the experimental data was used. When the flow was not reversed and was leaving the exit boundary, extrapolation of the boundary values from the interior cells was performed such that the continuitive condition was used $(\partial u/\partial x = 0)$. The computational results that follow were calculated using third-order accurate flux differencing for the interior cell faces.

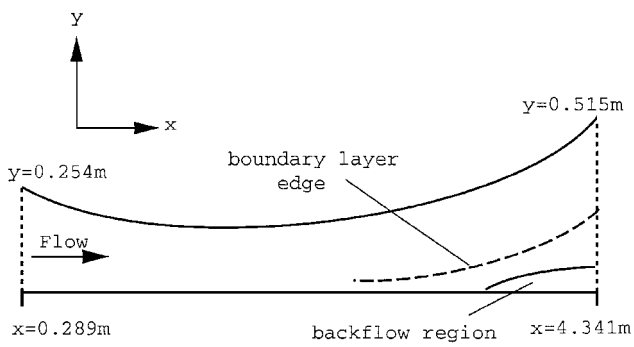

Fig. 1 Computational domain for the low-speed diffuser.

Results for the steady flow case are presented in Figs. 2–6. In all of the steady case plots, the experimental data are presented with the baseline JKM and BLM[16] turbulence model. The BLM is shown here for comparison and reveals the typical behavior of an equilibrium eddy viscosity formulation. Along with these two models, the modifications presented in the preceding section are also shown for the JKM. The modified JKM consists of the new ODE, Eq. (23), applied in the detached flow zone, the changes to the velocity scale parameter, and the inner eddy viscosity term given in Eq. (31). The normal stress model (26) for the x-momentum equation was not included with the other modifications. It was found from implementing the model with the baseline JKM that no noticeable improvements occurred. The eddy viscosity formulation for the Reynolds

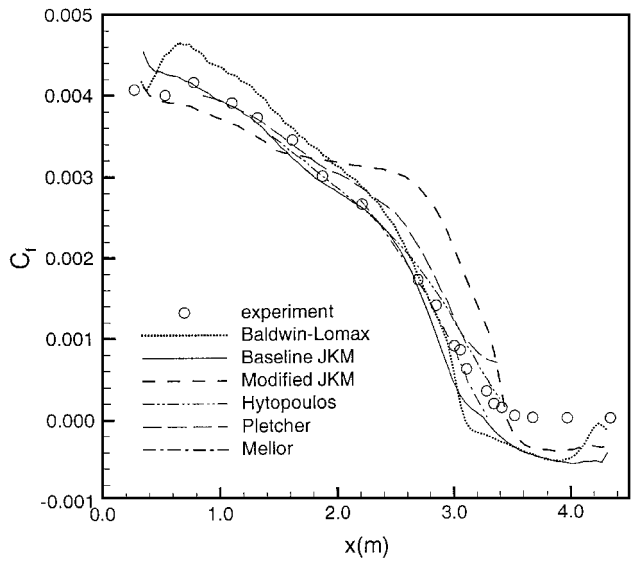

Fig. 2 Friction coefficient for the steady diffuser case.

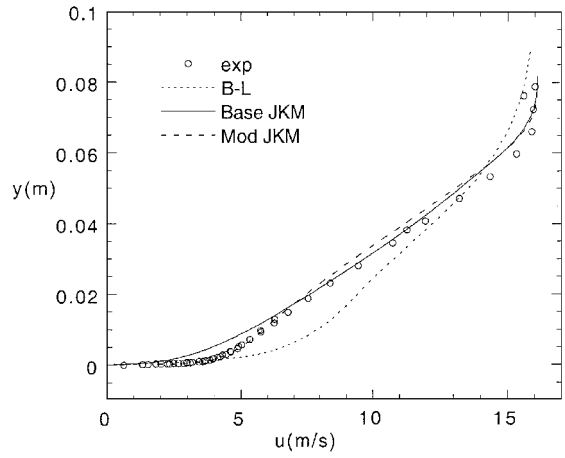

Fig. 3 Comparison of the steady diffuser boundary-layer profile at 3.01 m.

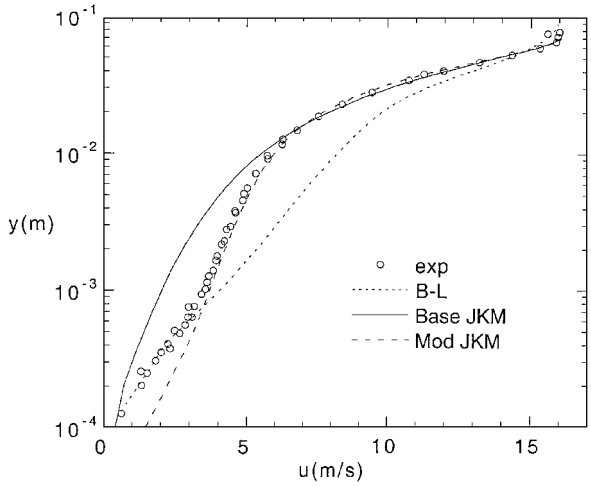

Fig. 4 Semilog scale comparison of the steady diffuser boundary-layer profile at 3.01 m.

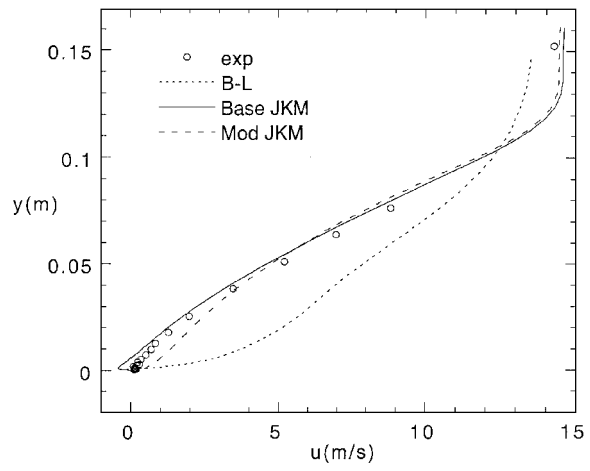

Fig. 5 Comparisons of the steady diffuser boundary-layer profile at 3.42 m.

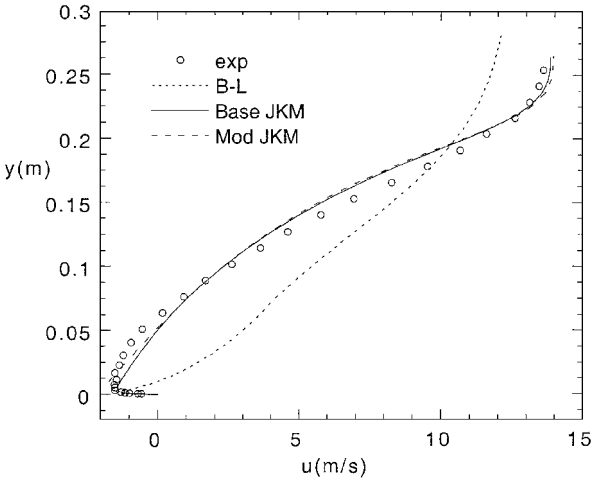

Fig. 6 Comparisons of the steady diffuser boundary-layer profile at 3.97 m.

shear stress dominated the turbulence modeling throughout the diffuser, and the effects from the normal stress model were not seen.

The skin-friction coefficient is shown in Fig. 2 Additional skin-friction values from other sources are also presented in Fig. 2 for comparison. The results from Pletcher et al. and Mellor et al. are taken from Ref. 17. The turbulence model used by Pletcher et al. (see Ref. 17) was based on a one-half equation model, where the velocity and length scales for the outer region are obtained from the TKE equation and an additional auxiliary equation. The turbulence model implemented by Mellor et al. used a five-equation Reynolds stress model. Results from Hytopoulos[18] are from a half-equation turbulence model based on Prandtl's mixing length. In a similar fashion to the JKM, the Hytopoulos model used an auxiliary equation to solve for the maximum Reynolds shear stress, which was then used to scale the Reynolds stress in the outer portion of the viscous shear layer. The results show that flow detachment is not easily predicted, and only two of the models are close to predicting the separation location correctly, the modified JKM and the Hytopoulos model.

The baseline JKM predicted C_f well for most of the flow leading up to the strong adverse pressure gradient. Near detachment, the baseline model tended to underpredict C_f, resulting in an early detachment location. The JKM modifications had a large impact on C_f. As the adverse pressure gradient increased, the skin-friction values did not decrease as fast as the experiment showed. Values of C_f remained high up to separation, where C_f then decreased rapidly to zero. This effect on C_f came mainly from the inner region pressure gradient term and the use of u^* as the velocity scale. These changes had a large impact on the eddy viscosity production near the wall, where C_f is sensitive to the velocity gradients. As separation approached, the pressure gradient tended to decrease as well, limiting the effect it had on the inner boundary layer region and causing the skin friction to go to zero rather rapidly. The increase in eddy viscosity production near the wall during the adverse pressure gradient caused the modified JKM to have less favorable agreement with the C_f data for that region, but it did delay the separation location, allowing good correlation with experiment farther downstream. The separation location occurred at 3.45 m for the modified JKM and 3.30 m for the baseline model. The addition of the pressure term in Eq. (31) had a large effect on moving the detachment location downstream, making the modified JKM have the closest agreement with experiment for the separation location of 3.55 m.

The mean velocity profiles at three streamwise locations are presented in Figs. 3–6. The profiles in Figs. 3 and 4 are in the region leading up to detachment, where the pressure gradient has become strong. In the experimental calculations, the normal stress terms at this location make up over 40% of the total production of energy. Figure 5 shows the mean velocity profile just before the detachment point, whereas Fig. 6 shows a velocity profile inside the backflow region.

The inner region modification to the JKM improved the velocity profile in the region leading up to flow detachment. It was in this region of the flow that the best improvement over the baseline JKM was found. A semilog plot of the velocity at 3.01 m is given in Fig. 4 to show how strong an effect the pressure gradient had on the inner region profile. The modified JKM follows the experimental data much more closely near the wall due to the added viscosity from Eq. (31). In the region after the detachment location, the baseline and modified models gave very similar profiles, both of which agreed well with the experimental data.

Computed Results: FFX

The FFX was designed to produce a two-dimensional flow around a stationary hydrofoil. A diagram of the experimental setup is shown in Fig. 7, where all dimensions have been nondimensionalized by the chord length. The vertical gusts imposed on the stationary hydrofoil were generated by two smaller hydrofoils known as the flappers. The flappers would undergo an oscillatory motion in which both flappers would rotate in phase. The sinusoidal gust loading imposed on the stationary foil was created by the vortex sheets being shed from the flappers. For more details on the experiment, see Refs. 19–21.

The upstream location of the experimental data in both the steady and unsteady computations is indicated by a dashed line in Fig. 7. This line of data is 0.259 chord lengths in front of the foil leading edge and fixes the inflow boundary location for the numerical simulation. The exit boundary location for both cases is located one chord length downstream from the foil trailing edge. The side walls of the computational domain were treated with the tangency boundary condition, whereas the outflow boundary used the continuitive condition. For the computational results that follow, an

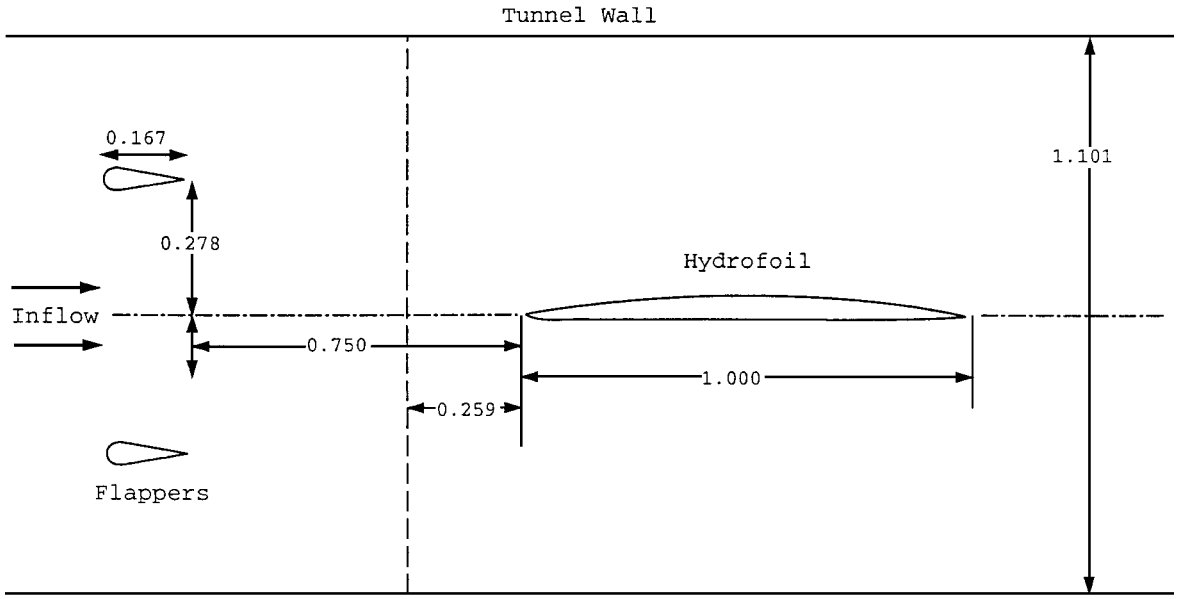

Fig. 7 Flapping foil experimental setup.

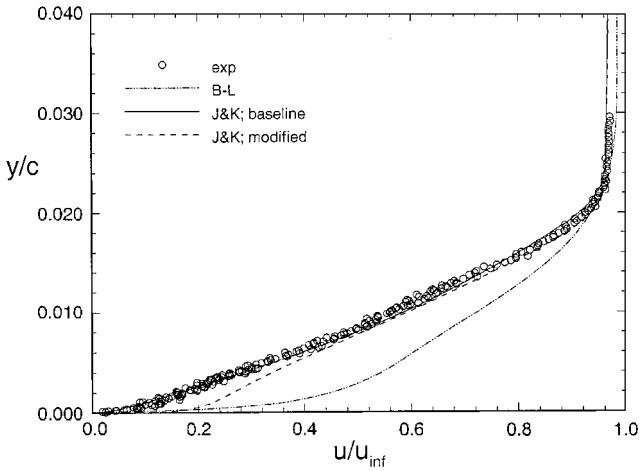

Fig. 8 FFX steady case velocity profile at $x/c = 0.972$.

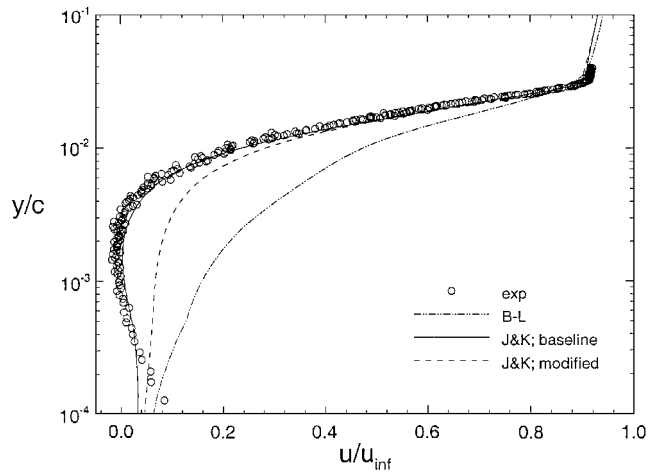

Fig. 9 FFX steady case velocity semilog profile at $x/c = 1.00$.

O grid was chosen for both the steady and unsteady cases. The grid has one direction of grid lines that begins on the hydrofoil surface and extend to the outer boundary, whereas the second grid direction forms a closed loop around the hydrofoil. A grid convergence study was performed using the following grids: (101 × 81), (121 × 101), (121 × 121), and (141 × 101). The boundary-layer displacement thickness, the boundary-layer edge velocity, and boundary-layer profiles were used to compare the grids. The (121 × 101) mesh was chosen for use in the following computational results.

Steady Flow Case

All cases were computed using $\beta = 1000$ and a Courant–Friedrichs–Lewy number of 30. For each iteration, two sweeps were done around the airfoil, one in the clockwise direction followed by a sweep in the opposite direction. The compressibility parameter β was varied from 500 to 5000 to see whether any changes in the solution occurred, but none were observed. For the JKMs, σ was allowed to start varying after the transition location. The lower (or pressure) surface was computed using equilibrium conditions.

Two boundary-layer profiles for the suction side are presented in Figs. 8 and 9. For each profile, the BLM overpredicted the eddy viscosity, which resulted in a thicker boundary layer. Both JKMs do an excellent job of predicting the boundary-layer profiles. For the profiles up to $x/c = 0.900$ (not shown), the correlation with experimental data was very good. For the region near the trailing edge, the baseline model does a better job overall of predicting the velocity. Near the wall, the modified JKM has an increased prediction of eddy viscosity. This is mainly a result of the pressure term added to the inner JKM model. As observed from the diffuser case, the pressure term tends to delay the detachment point. This was an improvement for the diffuser case but is not as necessary for the flapping foil problem discussed here.

The last profile at $x/c = 1.00$ shows the impact of the adverse pressure gradient that exists on the suction side. The flow has reattached at this point, but the velocity profile still reveals some backflow velocity. This type of flow presents a challenge to any turbulence model, yet the baseline JKM does an excellent job of matching the experimental data. To show the near-wall region even better, a semilog plot of the profile is given in Fig. 9.

Unsteady Flow Case

To make comparisons with the experimental data for the unsteady case, a Fourier analysis was performed. This allows the amplitude and phases of the harmonics to be calculated, along with their mean value. A more complete discussion of this can be found in Ref. 5.

For the time-accurate calculations, a time step was taken equivalent to one phase (180 phases per cycle). Several runs were made with the baseline model in which the number of subiterations was set to 50, 70, 100, and 140. This was done to test the number of inner iterations needed to be performed to properly satisfy conservation of mass. The solutions showed that 100 subiterations per physical time step were more than enough to properly satisfy continuity. The norm of the continuity equation was reduced to 10^{-4} or less. The parameter β was again held at 1000 as in the steady case, and

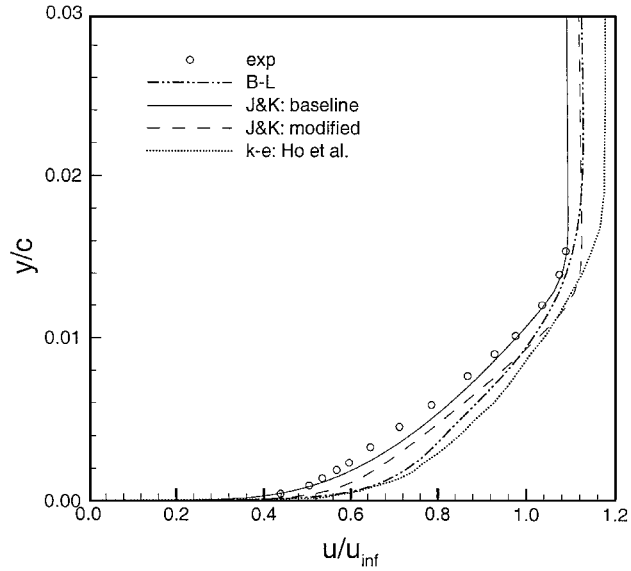

Fig. 10 Unsteady FFX mean velocity profiles at $x/c = 0.900$.

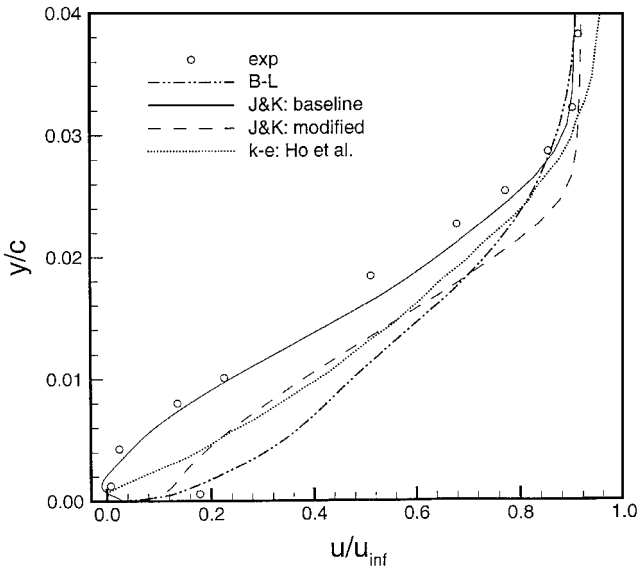

Fig. 11 Unsteady FFX mean velocity profiles at $x/c = 1.00$.

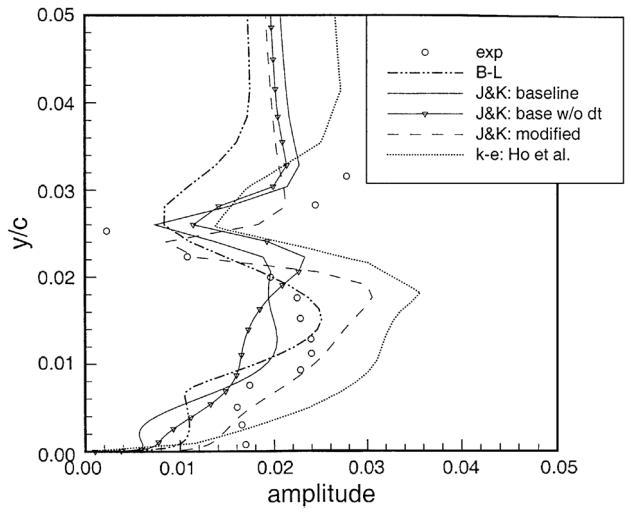

Fig. 12 Unsteady FFX amplitude data at $x/c = 0.990$.

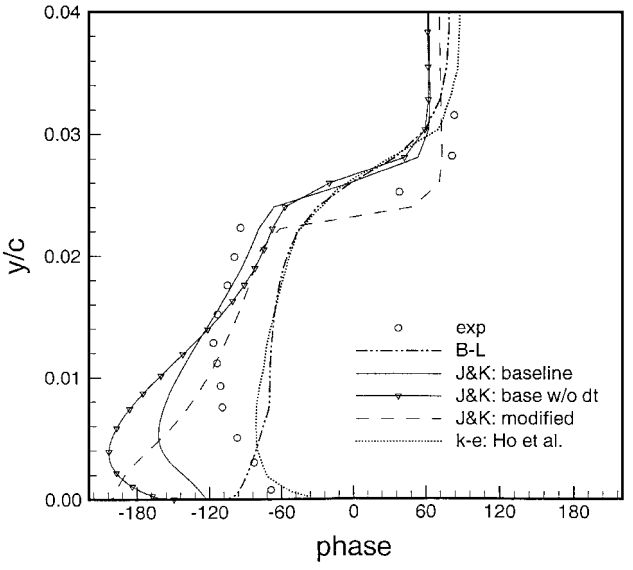

Fig. 13 Unsteady FFX phase data at $x/c = 0.990$.

the pseudotime step was set to a very large number ($\Delta\tau = 1 \times 10^{12}$) to ensure mass conservation for time accuracy.

The mean tangential boundary-layer velocity profiles are given in Figs. 10 and 11 for two stations along the upper foil surface. The amplitude and phase information at a single location is plotted in Figs. 12 and 13. In addition to the Baldwin–Lomax and Johnson–King turbulence models, computational results from Ho and Lakshminarayana[22] using the two-equation k–ϵ model are presented.

The baseline JKM had the best overall agreement with experiment for the mean velocity profiles. There are not as many experimental data points near the wall, but the baseline JKM seems to predict the correct amount of mean backflow velocity at x/c of 1.000. In the steady case, the modified JKM had similar performance to the baseline model for most of the profiles, but this was not the trend in the unsteady case. The modified model predicted higher velocities compared to experiment for most every location, especially near the trailing edge. The displacement thickness for the modified model tended to be closer to the BLM prediction. Neither the modified JKM nor BLM captured any of the backflow velocity that was occurring at the trailing edge. The k–ϵ model was the next closest model after the baseline JKM to agree with experiment.

For the profiles near the trailing edge, a distinct phase shift occurs near the edge of the boundary layer. This shift in the phase is also seen in the computational results. The modified JKM appears to have better agreement with the experiment than the baseline model. At the edge of the boundary layer, the baseline JKM is leading all of the other models and experimental data. Near the wall, both models tend to have a phase lead over the experimental data, but again the baseline model has the largest phase lead. The overall trend seen in the experiment for the amplitude data is reflected in the computations as well. The modified JKM had larger peaks in the amplitude over the baseline model. This increased sensitivity to the unsteady flow may be a large result of the inner eddy viscosity model being a function of the pressure gradient.

The time-dependent term in the Johnson and King differential equation was observed to have no effect on the velocity profiles in FFX, but a difference did appear near the trailing edge in the amplitude and phase plots. In Figs. 12 and 13, the baseline JKM without the time-dependent term given in Eq. (11) is plotted along with the other models. A larger phase difference near the wall appears to occur when the time-dependent Reynolds shear stress is not included in the differential equation. This was the only effect observed by removing the time dependency in the JKM.

Conclusions

The Johnson and King turbulence model was used to compare computational results with experimental data for a low-speed diffuser flow and the MIT FFX. Modifications were made to the model concerning the normal stress production in the differential

equation, and a model was also suggested for the Reynolds normal stress term in the momentum equation. In addition to these changes, a term was added to the inner region eddy viscosity model based on the pressure gradient. A different velocity scaling parameter was also suggested based on the local value of the Reynolds shear stress.

For the unsteady flow, the JKM had a time-dependent term associated with the differential equation used to scale the outer eddy viscosity. This time-dependent term was observed to have no impact on the velocity profiles in the FFX unsteady test case. However, the time dependency in the model did have an effect on the phase angle and amplitude for the boundary-layer profiles, but only in the vicinity of separation. The time dependency in the JKM auxiliary equation does not appear to be very important for determining the Reynolds-averaged mean flow values.

The largest impact to the JKM from the modifications was from the incorporation of a pressure gradient term into the inner eddy viscosity model. For the steady diffuser case, the changes to the model predicted flow detachment farther downstream, which compared more favorably with experiment. For the flapping foil case, the same effect also occurred such that the flow remained attached at the trailing edge instead of separating. For the unsteady flows, the pressure gradient term increased the sensitivity of the turbulence model to the unsteady flowfield, resulting in higher amplitudes in the velocity profiles.

For the normal stress model, which appears in the Reynolds-averaged x-momentum equation, a new model was formulated. Both the diffuser and FFX cases were calculated with the new model. The changes made to the turbulence modeling did not have any significant impact on the computational results for either test case. It appeared that the eddy viscosity model for the apparent Reynolds shear stress term dominated the turbulence modeling and prevented the new normal stress model from making any significant contributions to the mean flowfield.

The Johnson and King turbulence model, along with a modified version of the model, was demonstrated for two test cases involving strong adverse pressure gradients and separation. The original JKM correlated well with experimental data in both steady and unsteady flow conditions. The performance of this model from the time of its development to the present has continued to confirm that this model performs well for flows with separation. The modified version of this model was developed as an attempt to incorporate more of the flow physics of separated flow into the original formulation of the Johnson and King turbulence model. For the two test cases presented here, the modified JKM did not prove to be superior to the original JKM. In fact, for the unsteady flow test case, the modified version appeared to be inferior to the original model. The modifications, therefore, did not greatly improve the JKM. Instead, ideas were presented on how to modify turbulence models such as the JKM with hopes of improving turbulent flow calculations.

References

[1]Johnson, D. A., and King, L. S., "A Mathematically Simple Turbulence Closure Model for Attached and Separated Turbulent Boundary Layers," *AIAA Journal*, Vol. 23, No. 11, 1985, pp. 1684–1692.

[2]Menter, F. R., "Performance of Popular Turbulence Models for Attached and Separated Adverse Pressure Gradient Flow," AIAA 91-1784, June 1991.

[3]Simpson, R. L., Chew, Y.-T., and Shivaprasad, B. G., "The Structure of a Separating Turbulent Boundary Layer. Part I. Mean Flow and Reynolds Stresses," *Journal of Fluid Mechanics*, Vol. 113, 1981, pp. 23–51.

[4]Paterson, E., and Stern, F., "Computation of Unsteady Viscous Flow with Application to the MIT Flapping Foil Experiment," *Proceedings of the Sixth International Conference on Numerical Ship Hydrodynamics* (Iowa City, IA), National Academy Press, Washington, DC, 1993, pp. 669–720.

[5]Taylor, L., Busby, J. A., Jiang, M., Arabshahi, A., Sreenivas, K., and Whitfield, D., "Time Accurate Incompressible Navier–Stokes Simulation of the Flapping Foil Experiment," *Proceedings of the Sixth International Conference on Numerical Ship Hydrodynamics* (Iowa City, IA), National Academy Press, Washington, DC, 1993, pp. 721–738.

[6]Kiris, C., Rogers, S., Kwak, D., and Lee, Y., "Time Accurate Incompressible Navier–Stokes Computations with Overlapped Moving Grids," *Advances in Computational Methods in Fluid Dynamics*, American Society of Mechanical Engineers, New York, 1987, pp. 67–76.

[7]Yang, H. Q., Ho, S. Y., and Przekwas, A. J., "A Numerical Study of a Two-Dimensional Foil Subject to High Reduced Frequency Gust Loading," AIAA Paper 95-2266, June 1995.

[8]Rogers, S. E., and Kwak, D., "An Upwind Differencing Scheme for the Time-Accurate Incompressible Navier–Stokes Equations," *AIAA Journal*, Vol. 28, No. 2, 1990, pp. 253–262.

[9]Rogers, S. E., and Kwak, D., "Steady and Unsteady Solutions of the Incompressible Navier–Stokes Equations," *AIAA Journal*, Vol. 29, No. 4, 1991, pp. 603–610.

[10]Neel, R., Walters, R. W., and Simpson, R. L., "Computations of Steady and Unsteady Low-Speed Turbulent Separated Flows," AIAA Paper 97-0653, Jan. 1997.

[11]Johnson, D. A., and Coakley, T. J., "Improvements to a Nonequilibrium Algebraic Turbulence Model," *AIAA Journal*, Vol. 28, No. 11, 1990, pp. 2000–2003.

[12]Shiloh, K., Shivaprasad, B. G., and Simpson, R. L., "The Structure of a Separating Turbulent Boundary Layer. Part III. Transverse Velocity Measurements," *Journal of Fluid Mechanics*, Vol. 113, 1981, pp. 75–90.

[13]Simpson, R. L., Chew, Y.-T., and Shivaprasad, B. G., "The Structure of a Separating Turbulent Boundary Layer. Part II. Higher-Order Turbulence Results," *Journal of Fluid Mechanics*, Vol. 113, 1981, pp. 53–73.

[14]Huang, P. G., and Bradshaw, P., "Law of the Wall for Turbulent Flows in Pressure Gradients," *AIAA Journal*, Vol. 33, No. 4, 1995, pp. 624–632.

[15]Schetz, J. A., *Boundary Layer Analysis*, Prentice–Hall, Englewood Cliffs, NJ, 1993, pp. 233–237.

[16]Baldwin, B. S., and Lomax, H., "Thin Layer Approximation and Algebraic Model for Separated Turbulent Flows," AIAA Paper 78-257, Jan. 1978.

[17]Kline, S. J., Cantwell, B. J., and Lilley, G. M., "The 1980-81 AFOSR–HTTM–Stanford Conference on Complex Turbulent Flows: Comparison of Computation and Experiment," Thermosciences Div., Mechanical Engineering Dept., Stanford Univ., Stanford, CA, 1981.

[18]Hytopoulos, E., "A Turbulence Model for Steady and Unsteady Boundary Layers in Strong Pressure Gradients," Ph.D. Thesis, Dept. of Aerospace Engineering, Virginia Polytechnic Inst. and State Univ., Blacksburg, VA, 1994.

[19]Rice, J., "Investigation of a Two-Dimensional Hydrofoil in Steady and Unsteady Flows," M.S. Thesis, Dept. of Ocean Engineering, Massachusetts Inst. of Technology, Cambridge, MA, June 1991.

[20]Delpero, P. M., "Investigation of Flows Around a Two Dimensional Hydrofoil Subject to a High Reduced Frequency Gust Loading," M.S. Thesis, Dept. of Ocean Engineering, Massachusetts Inst. of Technology, Cambridge, MA, Feb. 1992.

[21]Lurie, E. A., "Investigation of High Reduced Frequency, Separated Trailing Edge Flows," Ph.D. Thesis, Dept. of Ocean Engineering, Massachusetts Inst. of Technology, Cambridge, MA, Sept. 1996.

[22]Ho, Y.-H., and Lakshminarayana, B., "Computation of Unsteady Flowfield over a Hydrofoil, Including Boundary Layer and Wake," *AIAA Journal*, Vol. 35, No. 1, 1997, pp. 40–50.

F. W. Chambers
Associate Editor